Engineering Analysis with Boundary Elements 171 (2025) 106057

Contents lists available at ScienceDirect

Engineering Analysis with Boundary Elements

journal homepage: www.elsevier.com/locate/enganabound

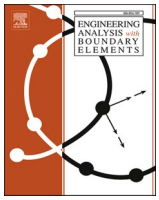

Sphere elements in the BEM for the analysis of elastic bodies with spherical voids or inclusions

Yong-Tong Zheng [a,b], Yijun Liu [b], Xiao-Wei Gao [c], Wei-Zhe Feng [c,*]

[a] School of Infrastructure Engineering, Nanchang University, 330031, China
[b] Department of Mechanics and Aerospace Engineering, Southern University of Science and Technology, Shenzhen 518055, China
[c] School of Mechanics and Aerospace Engineering, Dalian University of Technology, Dalian 116024, China

ARTICLE INFO

Keywords:
Boundary element method
Sphere elements
Isoparametric closure elements
Porous materials
Particle embedded materials

ABSTRACT

In this paper, a series of novel sphere elements are proposed in the boundary element method (BEM). These elements are designed as isoparametric closure elements to simulate spherical geometries with greater accuracy and fewer nodes than conventional boundary elements. Constructed similarly to multi-dimensional Lagrange elements, these sphere elements utilize trigonometric bases for each dimension. To avoid zero Jacobians at polar nodes, poleless sphere elements combined with triangular elements are employed to approximate spheres. The evaluation methods of boundary integrals over these elements, including singular and nearly singular integrals, are derived using degenerated element techniques and adaptive subdivision techniques, respectively. Three numerical examples are employed to underscore the advantages of the proposed elements, showing that with only 50 nodes per sphere, results align closely with those obtained using 290 nodes per sphere with conventional boundary elements, effectively reducing degrees of freedom without sacrificing accuracy.

1. Introduction

Spherical voids and inclusions are commonly observed in materials like porous and particle-embedded materials. Whatever purpose these sphere geometries are designed for, the displacement and stress distribution in the vicinity will be altered and these voids and inclusions will result in stress concentration. Generally, to obtain the distribution of stresses and displacements over complex geometries, numerical methods are the mainstream options, such as the finite element method [1–3] (FEM) and boundary element method [4–6] (BEM). If considering the structures with a lot of spherical voids or inclusions, BEM may have advantages in mesh generation because it does not need to discretize inner space of the computational domain. Furthermore, boundary integral equations (BIEs) contain no derivate term of displacement, resulting in more accurate results. Nevertheless, numerous elements and nodes are still necessary in approximating spherical geometries and interpolating the stresses and displacements over the surfaces, which may lead to high computational costs when the number of spheres increases.

To address spherical geometry discretization efficiently, various researchers have developed specialized boundary elements and associated techniques. Feng et al. designed three types of quadratic interpolation elements for acoustic BEM, stating that their discretization techniques directly represent the actual spherical surface geometry without geometrical error [7]. However, accurately capturing sound pressure gradients with this approach still required a high number of elements and nodes. Gao et al. introduced a series of isoparametric closure elements based on Lagrange interpolation for elasticity BEM, including sphere elements [8–10]. These sphere elements effectively model complete spherical geometries, reducing the number of degrees of freedom (DOFs) needed for spherical voids and inclusions. Nevertheless, their accuracy in stress evaluation, particularly at the end nodes and polar nodes, remains limited. To improve smoothness at the end nodes, Ma et al. developed smooth sphere elements by reusing real nodes as auxiliary nodes along latitude and longitude directions [11,12]. While the issue of polar nodes persists, their approach indeed enhances both smoothness and accuracy at end nodes, although further improvements may still be possible.

Beyond Lagrange interpolation, other researchers have explored hole-like elements based on trigonometric functions. Banerjee and Henry et al. proposed a 3-node element utilizing trigonometric-based shape functions for thermal, mechanical, and thermoelastic analyses of composites with voids and fiber inclusions [13–16]. By accounting for geometric characteristics, their approach simplified boundary integral

* Corresponding author.
E-mail address: wzfeng@dlut.edu.cn (W.-Z. Feng).

https://doi.org/10.1016/j.enganabound.2024.106057
Received 4 July 2024; Received in revised form 29 October 2024; Accepted 28 November 2024
Available online 6 December 2024

equations (BIEs) and reduced computational costs. Buroni et al. constructed 4-, 5-, and 6-node trigonometric hole elements to model cylindrical voids in computational domains [17,18]. However, their methods did not address near-singular integral evaluations over these elements, limiting their application in cases with closely spaced voids. Zhang et al. developed a tube element based on a 3-node hole element and integrated it with the boundary face method to address problems in heat conduction, mechanics, and acoustics [19–21]. Zheng et al. constructed higher-order Lagrange and trigonometric hole elements with variable node counts, ultimately concluding that trigonometric interpolation is more effective for hole elements after a detailed comparison of 31 element types [22].

In summary, previous sphere elements [8–11] have shown limitations in accurately modeling spherical geometries, particularly at end nodes and polar nodes. Additionally, prior studies indicated that trigonometric interpolation is better suited than Lagrange interpolation for circular geometries. In response, this paper introduces new elements designed to model spherical geometries in mechanics problems, drawing from Gao's construction methods [9] and employing trigonometric interpolation along latitude and longitude directions. This approach effectively improves the smoothness at end nodes. To address the issue of a zero Jacobian at polar nodes, poleless sphere elements are combined with several triangular elements to discretize spherical geometries. The degenerated element method is applied to evaluate weakly singular integrals over the proposed elements, while an adaptive element subdivision method handles near-singularities. Finally, three numerical examples are provided to demonstrate the accuracy and efficiency of the proposed elements.

The rest of the paper is organized as follows. Section 2 provides an overview of the basic BEM formulations for mechanics problems. Section 3 reviews the construction methods of the Lagrange sphere elements proposed by Gao and Ma and primarily introduces the novel sphere elements. Section 4 details the methods for evaluating singular and nearly singular integrals over the proposed sphere elements. Section 5 presents three numerical examples and their results. Finally, Section 6 offers concluding remarks.

2. Briefly introduction of the BEM

For three-dimensional elasticity problems within a domain Ω and its boundary Γ, the boundary integral equation (BIE) for the displacement field can be expressed as follows [4–6]:

$$c_{ij}u_j(P) = \int_\Gamma u_{ij}^*(P,Q)t_j(Q)\mathrm{d}\Gamma(Q) - \mathrm{CPV}.\int_\Gamma t_{ij}^*(P,Q)u_j(Q)\mathrm{d}\Gamma(Q), \tag{1}$$

where the notation CPV.$\int$ signifies that the integral is to be interpreted in the Cauchy principal value sense. Here, P and Q denote the source and field points, respectively, while u_j and t_j represent displacement and surface traction, respectively. The coefficient c_{ij} depends on the local geometry at P, equaling 0.5 for a smooth boundary and 1 when P is within the computational domain. The terms u_{ij}^* and t_{ij}^* are Kelvin's fundamental solutions, mainly determined by the distance between the source point and the field point (represented by r), and can be written as:

$$u_{ij}^* = \frac{1}{16\pi(1-\nu)\mu r}\left[(3-4\nu)\delta_{ij} + \frac{\partial \mathbf{r}}{\partial x_i}\frac{\partial \mathbf{r}}{\partial x_j}\right], \tag{2}$$

$$t_{ij}^* = -\frac{1}{8\pi(1-\nu)r^2}\left\{\frac{\partial \mathbf{r}}{\partial \mathbf{n}}\left[(1-2\nu)\delta_{ij} + 3\frac{\partial \mathbf{r}}{\partial x_i}\frac{\partial \mathbf{r}}{\partial x_j}\right] + (1-2\nu)\left(n_i\frac{\partial \mathbf{r}}{\partial x_j} - n_j\frac{\partial \mathbf{r}}{\partial x_i}\right)\right\}. \tag{3}$$

in which μ is the shear modulus, ν the Poisson ratio, and x_i denotes the coordinate in the i th orientation. The vector $\mathbf{r}$ extends from the source point to the field point, $\mathbf{n}$ is the outward normal at field point Q, and n_i are the components of vector $\mathbf{n}$. Here, δ_{ij} is the Kronecker delta. Subscripts i and j follow the Einstein summation convention (the same hereinafter).

The BIE for stress can be expressed as follows:

$$\sigma_{ij}(P) = \int_\Gamma U_{ijk}{}^*(P,Q)t_k(Q)\mathrm{d}\Gamma(Q) - \int_\Gamma T_{ijk}^*(P,Q)u_k(Q)\mathrm{d}\Gamma(Q), \tag{4}$$

where U_{ijk}^* and T_{ijk}^* can be calculated by following two formulas:

$$U_{ijk}^* = \frac{1}{8\pi(1-\nu)r^2}\left[(1-2\nu)\left(\delta_{ik}\frac{\partial \mathbf{r}}{\partial x_j} + \delta_{jk}\frac{\partial \mathbf{r}}{\partial x_i} - \delta_{ij}\frac{\partial \mathbf{r}}{\partial x_k}\right) + 3\frac{\partial \mathbf{r}}{\partial x_i}\frac{\partial \mathbf{r}}{\partial x_j}\frac{\partial \mathbf{r}}{\partial x_k}\right], \tag{5}$$

$$\begin{aligned} T_{ijk}^* = \frac{\mu}{4\pi(1-\nu)r^3}\Bigg\{ & 3\frac{\partial \mathbf{r}}{\partial \mathbf{n}}\left[(1-2\nu)\delta_{ij}\frac{\partial \mathbf{r}}{\partial x_k} + \nu\left(\delta_{ik}\frac{\partial \mathbf{r}}{\partial x_j} + \delta_{jk}\frac{\partial \mathbf{r}}{\partial x_i}\right) - 5\frac{\partial \mathbf{r}}{\partial x_i}\frac{\partial \mathbf{r}}{\partial x_j}\frac{\partial \mathbf{r}}{\partial x_k}\right] \\ & + 3\nu\left(n_i\frac{\partial \mathbf{r}}{\partial x_j}\frac{\partial \mathbf{r}}{\partial x_k} + n_j\frac{\partial \mathbf{r}}{\partial x_i}\frac{\partial \mathbf{r}}{\partial x_k}\right) + (1-2\nu)\left(3n_k\frac{\partial \mathbf{r}}{\partial x_i}\frac{\partial \mathbf{r}}{\partial x_j} + n_j\delta_{ik} + n_i\delta_{jk}\right) - (1-4\nu)n_k\delta_{ij}\Bigg\} \end{aligned}. \tag{6}$$

Usually, Boundary Γ requires discretization into elements to evaluate boundary integrals in Eqs.(1) and (4). Within these elements, the displacements, surface tractions and geometries are interpolated in the same way, i.e.

$$u_i(\xi,\eta) = N_\alpha(\xi,\eta)u_i^\alpha, \tag{7}$$

$$t_i(\xi,\eta) = N_\alpha(\xi,\eta)t_i^\alpha, \tag{8}$$

$$x_i(\xi,\eta) = N_\alpha(\xi,\eta)x_i^\alpha, \tag{9}$$

in which N_α are the shape functions; α denotes the α-th node, and the repeated subscript α also follows Einstein summation convention. Intrinsic coordinates ξ and η range from -1 to 1. In a more rigorous sense, Eq. (8) for surface traction interpolation is optimal for flat elements, but is adapted in this paper for sphere elements due to extensive validation and minimal resulting error. For curved boundary elements, more rigorous formulations can be found in Refs. [23–25]. In this paper, all elements are isoparametric elements, including the new proposed sphere elements.

After discretizing the boundaries of the computational domain, let n_e represent the number of elements, Eqs.(1) and (4) can then be expressed in a discretized form:

$$\begin{aligned} c u_i(P) = & \sum_{e=1}^{n_e}\left\{t_j^\alpha\int_{-1}^{1}\int_{-1}^{1}u_{ij}^*(P,\xi_e,\eta_e)N_\alpha(\xi_e,\eta_e)J(\xi_e,\eta_e)d\xi_e d\eta_e\right\} \\ & - \sum_{e=1}^{n_e}\left\{u_j^\alpha\int_{-1}^{1}\int_{-1}^{1}t_{ij}^*(P,\xi_e,\eta_e)N_\alpha(\xi_e,\eta_e)J(\xi_e,\eta_e)d\xi_e d\eta_e\right\} \end{aligned}, \tag{10}$$

$$\sigma_{ij}(P) = \sum_{e=1}^{n_e} \left\{ t_k^{\alpha} \int_{-1}^{1} \int_{-1}^{1} U_{ijk}^{*}(P, \xi_e, \eta_e) N_{\alpha}(\xi_e, \eta_e) J(\xi_e, \eta_e) d\xi_e d\eta_e \right\} - \sum_{e=1}^{n_e} \left\{ u_k^{\alpha} \int_{-1}^{1} \int_{-1}^{1} T_{ijk}^{*}(P, \xi_e, \eta_e) N_{\alpha}(\xi_e, \eta_e) J(\xi_e, \eta_e) d\xi_e d\eta_e \right\}, \tag{11}$$

in which J represents the Jacobian. The standard BEM analysis process involves first assembling equations based on Eq. (10). Typically, for three-dimensional problems, each boundary node generates three equations. This results in an algebraic system:

$$[H]\{u\} = [G]\{t\}, \tag{12}$$

in which $\{u\}$ and $\{t\}$ represent the vectors containing the displacements and surface tractions at all boundary nodes, respectively. $[H]$ and $[G]$ are the coefficient matrices. Solving this linear algebraic system provides the displacements and surface tractions on the boundaries. These results can then be substituted into Eqs. (10) and (11) to obtain the displacements and stresses at any point within the computational domain. It should be noted that in this study, the stresses of the boundary nodes are evaluated using the traction recovery method [6], rather than using the stress BIE.

Most integrals in this process are evaluated using Gauss quadrature. However, when the source point P lies on or near the element e, the integrals in Eqs.(10) and (11) must be specially treated because they possess singularity or near-singularity, respectively. In this study, the rigid body motion method [6] is applied to avoid strongly singular integrals associated with the diagonal elements in the matrix $[H]$. As for weak-singular and near-singular integrals over the new proposed sphere elements, some special treatments must be applied, which are shown in Section 4 in detail.

3. Construction of isoparametric sphere elements

This section details the construction methods for isoparametric sphere elements. First, the construction of isoparametric hole elements, foundational to sphere elements, is briefly introduced. Next, semi-hole elements are developed. Sphere elements are then constructed by multiplying the hole and semi-hole elements along two orthogonal orientations. Finally, to address the zero Jacobian issues at polar nodes, poleless sphere elements are proposed.

3.1. Isoparametric hole elements

The shape functions of conventional Lagrange elements rely on a series of polynomials based on terms 1, ξ, ξ^2, ξ^3, and so on. Generally, circular boundaries are segmented into several Lagrange elements to approximate circular geometries with multiple low-order polynomial interpolations, though this requires a lot of nodes and elements to achieve high accuracy. To reduce the number of nodes, based on the characteristics of the circle, trigonometric functions, such as 1, cos θ, sin θ, $\cos^2\theta$ and so on, are introduced to replace the polynomial bases. Thus, a new coordinate system θ is established, with the relationship between ξ and θ defined as follows:

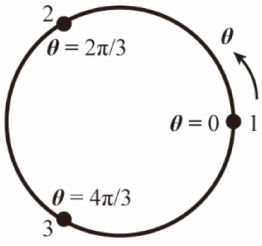

Fig. 1. 3-node trigonometric hole element [22].

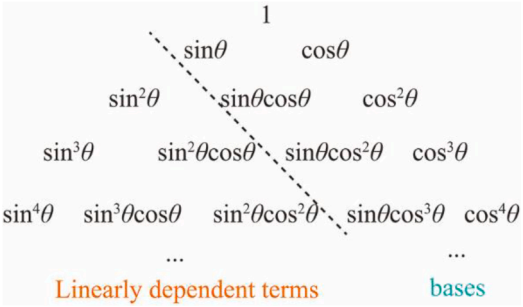

Fig. 2. Pascal triangle for selecting the bases.

$$\theta = \pi(1+\xi)\xi \in [-1,1]\theta \in [0, 2\pi]. \tag{13}$$

In trigonometric hole elements, nodes are evenly distributed around the circumference. For example, in a 3-node trigonometric hole element, the nodes are positioned at $\theta = 0$, $2\pi/3$, and $4\pi/3$, as shown in Fig. 1. The coefficients for bases such as 1, cos θ, sin θ, $\cos^2\theta$ within the shape functions are determined by solving equations based on the Kronecker delta property of the shape functions, with the detailed process provided in Ref. [22].

In cases where a 3-node element does not meet accuracy requirements, higher-order bases are used to construct hole elements with more nodes. However, due to the linear dependence of trigonometric functions, selecting higher-order bases is not as straightforward as that with polynomial bases. Fig. 2 illustrates a Pascal triangle composed of trigonometric functions, where only terms on the right side of the dotted line are chosen as bases. Terms on the left are excluded due to their linear dependence on those on the right. Shape functions for trigonometric hole elements with additional nodes are provided in Ref. [22].

3.2. Semi-hole elements

Extending the construction approach of hole elements to more generalized cases, elements representing semicircles can be developed similarly. For instance, a 5-node semi-hole element features five equally spaced nodes, as shown in Fig. 3. The relationship between coordinate systems ψ and η is written as follows:

$$\psi = \frac{\pi}{2}\eta\eta \in [-1,1]\psi \in \left[-\frac{\pi}{2}, \frac{\pi}{2}\right]. \tag{14}$$

Based on the previously introduced Pascal triangle, five trigonometric bases are selected as 1, cos ψ, sin ψ, $\cos^2\psi$, cos ψ·sin ψ. After determining the coefficients using the Kronecker delta property, the resulting shape functions can be written as follows:

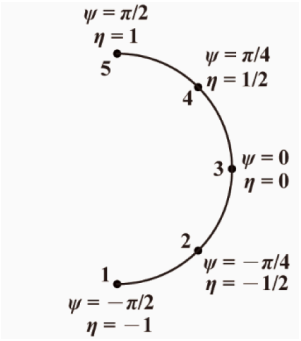

Fig. 3. 5-node semi-hole element.

$$\begin{cases} N_1(\psi) = 0.5\left(-1+\sqrt{2}\cos\psi\right)(-1+\cos\psi+\sin\psi) \\ N_2(\psi) = -\cos\psi\left(-1-\sqrt{2}+\left(1+\sqrt{2}\right)\cos\psi+\sin\psi\right) \\ N_3(\psi) = \left(1+\sqrt{2}\right)\cos\psi\left(-1+\sqrt{2}\cos\psi\right) \\ N_4(\psi) = \cos\psi\left(1+\sqrt{2}-\left(1+\sqrt{2}\right)\cos\psi+\sin\psi\right) \\ N_5(\psi) = 0.5\left(-1+\sqrt{2}\cos\psi\right)(-1+\cos\psi-\sin\psi) \end{cases} . \quad (15)$$

Similarly, semi-hole elements with an arbitrary number of nodes (exceeds 3) can be constructed in this way. Appendix A includes figures and shape functions for 3-node and 9-node semi-hole elements, providing additional examples.

3.3. Constructions of sphere elements

Sphere elements, characterized by two dimensions—longitude and latitude—are applied within three-dimensional BEM contexts. Latitude is represented by coordinate ξ and longitude by coordinate η, with θ and ψ coordinates following the relationships defined by Eqs. (13) and (14). Sphere elements are constructed by positioning hole and semi-hole elements at two orthogonal orientations and multiplying the shape functions of their corresponding nodes. The shape functions of two polar nodes are equal to those of two end nodes on the semi-hole elements. As an example, a 26-node sphere element is formed by combining an 8-node hole element with a 5-node semi-hole element, as shown in Fig. 4. The shape functions for all nodes are expressed as follows:

$$\begin{cases} N_1(\psi) = 0.7462+\cos\psi(-1.7276+0.9814\cos\psi+0.8382\sin\psi)-0.6374\sin\psi \\ N_2(\psi) = -0.5405+\cos\psi(3.9958-3.4552\cos\psi-1.2747\sin\psi)+0.1994\sin\psi \\ N_3(\psi) = 0.5886+\cos\psi(-4.5363+4.9477\cos\psi) \\ N_4(\psi) = -0.5405+\cos\psi(3.9958-3.4552\cos\psi+1.2747\sin\psi)-0.1994\sin\psi \\ N_5(\psi) = 0.7462+\cos\psi(-1.7276+0.9814\cos\psi-0.8382\sin\psi)+0.6374\sin\psi \end{cases} . \quad (18)$$

$$N_\alpha(\xi,\eta) = \begin{cases} C_\alpha(\xi)L_2(\eta) 1 \le \alpha \le 8 \\ C_{\alpha-8}(\xi)L_3(\eta) 9 \le \alpha \le 16 \\ C_{\alpha-16}(\xi)L_4(\eta) 17 \le \alpha \le 24 \\ L_1(\eta)\alpha = 25 \\ L_5(\eta)\alpha = 26 \end{cases}, \quad (16)$$

in which C_a represents the shape functions of the a-th node in the hole element, and L_b represents those of the b-th node in the semi-hole element. Generally, the positive directions of axis ξ and η shown in Fig. 4 indicate the outward normal of the sphere element pointing away from the sphere center, according to the right-hand rule. If the outward normal points toward the sphere center, either the ξ-axis or η-axis should be reversed.

In addition to the 26-node sphere element, 6-node, 14-node, 62-node, and 114-node sphere elements can be constructed in the same manner, as shown in Fig. 5. For these sphere elements, if all nodes are situated on a spherical surface, any point corresponding to a combination of ξ and η coordinates will also be located on that surface. However, the Jacobian values at the two polar nodes are zero, potentially causing significant errors near the poles. Overall, these sphere elements provide highly accurate geometric representations of entire spheres, except in the regions near the poles.

3.4. Poleless sphere elements

Poleless sphere elements are introduced to address issues at the poles in traditional sphere elements. This method avoids discretizing the regions near the poles by using triangular elements for these areas, enabling the construction of an entire spherical surface without the complications introduced by polar nodes.

The construction of poleless sphere elements begins with 2D arc elements. Fig. 6 shows a 5-node arc element, which is created by indenting two ends of a 5-node semi-hole element by a small angle θ (set to $\pi/20$ in this paper). The coordinate ψ is slightly modified for this element and can be expressed as follows:

$$\psi = \frac{9\pi}{20}\eta \quad \eta \in [-1,1] \quad \psi \in \left[-\frac{9\pi}{20}, \frac{9\pi}{20}\right]. \quad (17)$$

The shape functions are derived in the same manner as those for semi-hole elements:

Poleless sphere elements are constructed by combining hole elements with arc elements, where the shape functions are obtained by multiplying those of the corresponding nodes. The method for determining the outward normal follows that of the standard sphere elements, with the distinction that poleless sphere elements lack polar nodes. As illustrated in Fig. 7, a 40-node poleless sphere element, constructed from an 8-node hole element and a 5-node arc element, has an outward normal directed away from the spherical center. his design eliminates the zero Jacobian issues at the poles but introduces two new concerns. First, triangular elements may introduce slight geometric errors because an arbitrary point within the element may not exactly lie on the spherical surface. Nevertheless, if the angle θ is not too large (such as $\pi/20$ in this paper), the error remains negligible. The second concern is a

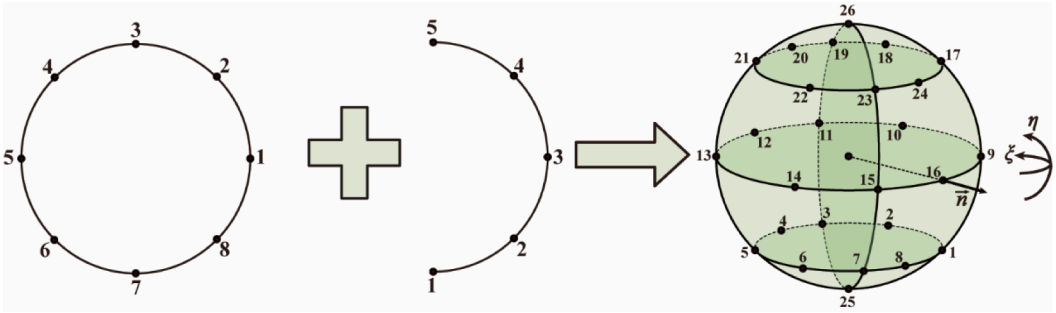

Fig. 4. Construction of a 26-node sphere element.

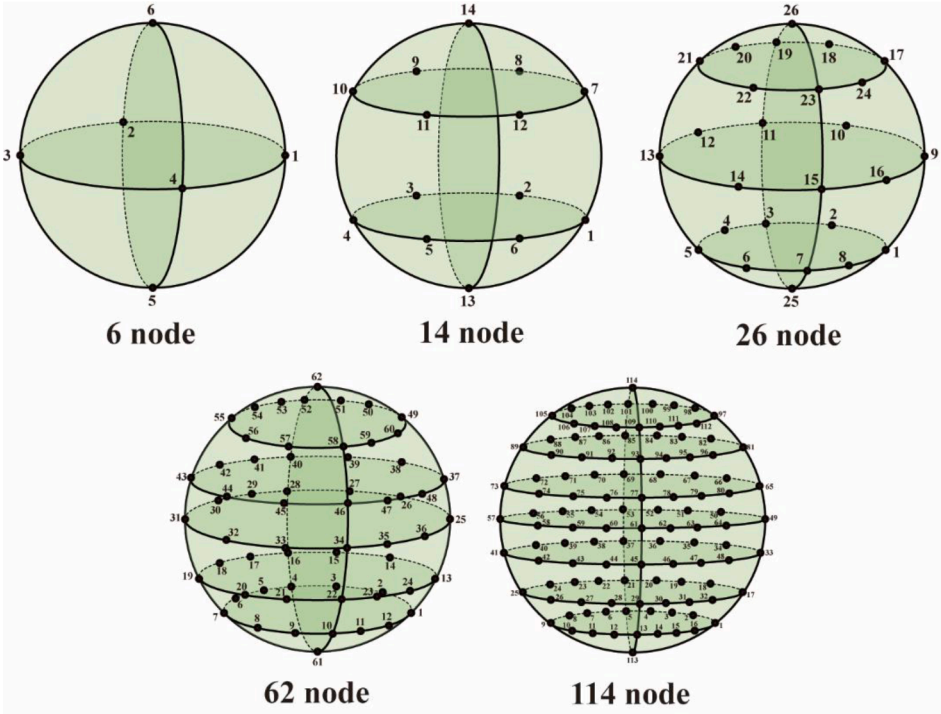

Fig. 5. 6-node, 14-node, 26-node, 62-node and 114-node sphere elements.

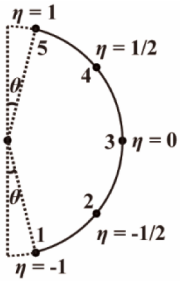

Fig. 6. A 5-node arc element.

modest increase in node count due to the poleless configuration. However, when targeting comparable accuracy, the total node count required to model a sphere remains lower than that with multiple conventional 8-node quadratic boundary elements. Both of them are verified in the following examples.

In this paper, three element-matching configurations will be employed to discretize the sphere: a 12-node (4 × 3) poleless sphere element matched with 8 linear triangular elements (14 nodes in total for the sphere), a 40-node (8 × 5) poleless sphere element matched with 8 quadratic triangular elements (50 nodes for the sphere), and an 84-node (12×7) poleless sphere element matched with 12 quadratic triangular elements (98 nodes for the sphere). These three configurations are shown in Fig. 8.

4. Evaluation of singular integrals over the sphere element

This section focuses on the treatment of weakly singular and near-singular integrals over the proposed sphere elements.

4.1. Weak-singular integral

According to the Eq. (10), the weak-singular integrals can be written as follows:

$$I_w = \int_{-1}^{1}\int_{-1}^{1} \frac{G_w(\xi,\eta)N_\alpha(\xi,\eta)J(\xi,\eta)}{r(\xi,\eta)}d\xi d\eta, \tag{19}$$

in which G_w represents the regular multiplier in the fundamental solution, i.e.

$$G_w = \frac{1}{16\pi(1-\nu)\mu}\left[(3-4\nu)\delta_{ij} + \frac{\partial \mathbf{r}(\xi,\eta)}{\partial x_i}\frac{\partial \mathbf{r}(\xi,\eta)}{\partial x_j}\right]. \tag{20}$$

In this paper, degenerate element method [6] is employed to deal with the weak-singular integrals. Unlike its use for conventional

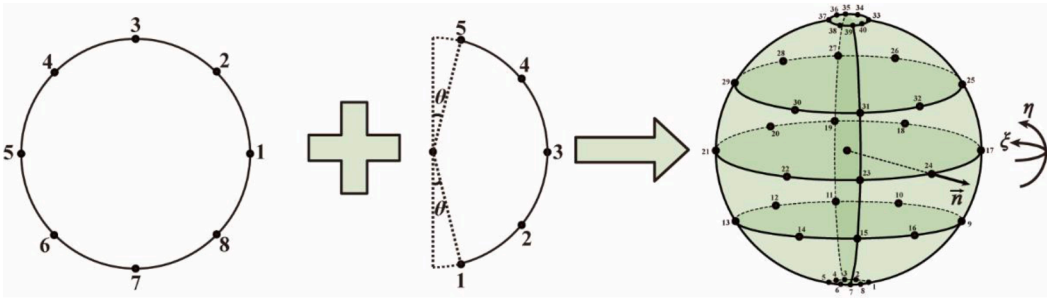

Fig. 7. Construction of a 40-node poleless sphere element.

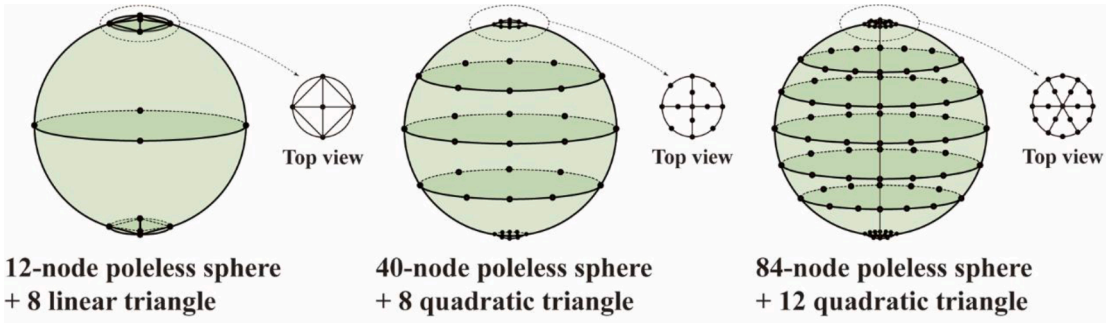

Fig. 8. Three matching configurations of the poleless sphere and triangular elements.

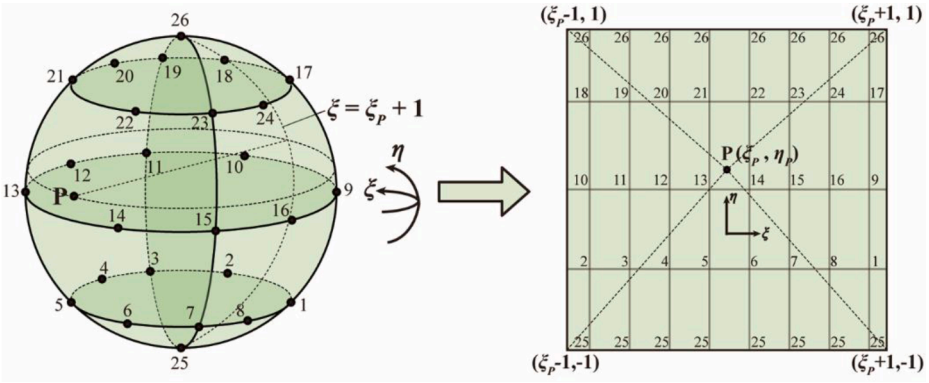

Fig. 9. Mapping a sphere element to a square.

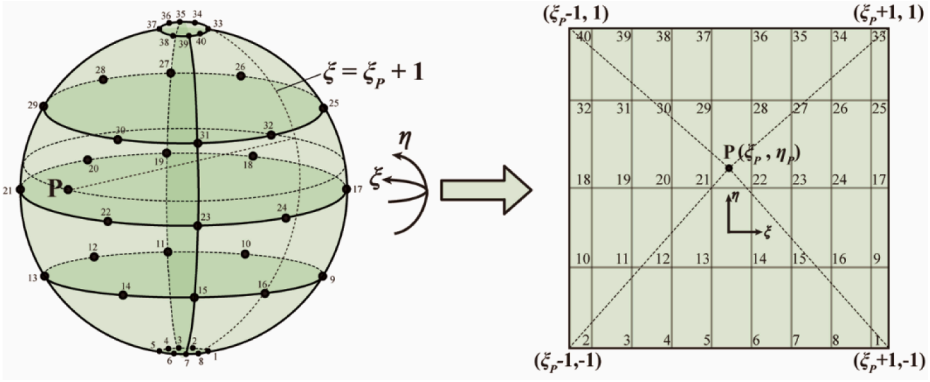

Fig. 10. Mapping a poleless sphere element to a square.

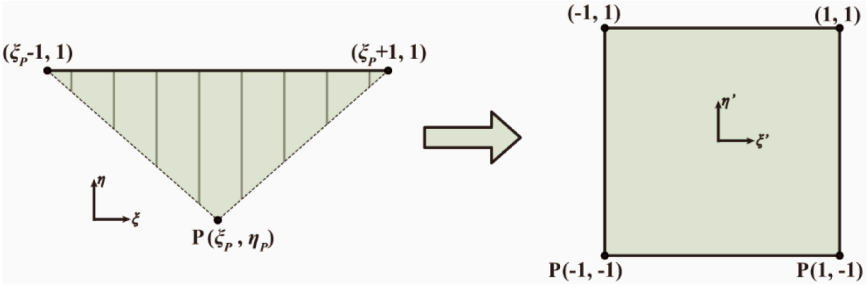

Fig. 11. Mapping the upper triangle to a square.

boundary elements, an additional procedure is required for the proposed sphere elements.

First, both sphere and poleless sphere elements are mapped onto a square, as shown in Figs. 9 and 10. This mapping involves "cutting" the spherical surface along its longitude line $\xi = \xi_P + 1$ or $\xi = \xi_P - 1$, which is opposite to the source point, then unfolding it, and stretching it into a square. During this process, it can be found that the sphere element degenerates at two poles because the poles are mapped to the edges of square in the parameter space. The resulting square is then subdivided into four triangles by connecting the source point to four vertices of the

square. Each triangle can subsequently be mapped to a square, where the source point corresponds to two nodes to eliminate the singularity [6], as shown in Fig. 11 (showing the mapping of the upper triangle). To describe it in a formula, the weak-singular integral becomes:

$$\int_{-1}^{1}\int_{-1}^{1}\frac{G_w N_\alpha J}{r}\mathrm{d}\xi\mathrm{d}\eta=\sum_{i=1}^{4}\int_{T_i}\frac{G_w N_\alpha J}{r}\mathrm{d}\xi\mathrm{d}\eta=\sum_{i=1}^{4}\int_{-1}^{1}\int_{-1}^{1}\frac{G_w N_\alpha J\cdot J_{T_i}}{r}\mathrm{d}\xi'\mathrm{d}\eta', \tag{21}$$

in which J_{T_i} is the Jacobian mapping from the triangle to the rectangle. The Jacobian approaches zero near the source point P, thereby eliminating the weak singularity by exploiting the properties of the degenerate element. This approach can also be viewed as effectively distributing more Gauss integration points around the source point.

4.3. Near-singular integrals

When the source point is near, but not on, the element, the singular terms r^{-1}, r^{-2} or r^{-3} in integrands will change drastically, which may lead to inaccurate evaluations of Gauss-Legendre quadrature, resulting in a near-singularity issue. To address this, in this paper, the subdivision method is used in this study to evaluate near-singular integrals. Before introducing the subdivision method [26], two points require clarification.

First, what is 'close' should be defined. In this paper, near-singularity is assessed following the criterion in Ref. [6], which can be written as:

$$r_{\min}\le\frac{L}{4}\left(\frac{e}{2}\right)^{-p/(2m)}, \tag{22}$$

in which $r_{\min}$ represents the distance from the source point to the element; L represents the element's actual length; e is the preset maximum integral error; m is the maximum allowable number of Gauss points; p is determined by the singularity order λ of the integrand, which can be expressed as follows:

$$p=\sqrt{\frac{2}{3}\lambda+\frac{2}{5}}. \tag{23}$$

Second, the method for calculating $r_{\min}$, the minimum distance from an arbitrarily positioned source point P to the sphere element, differs from conventional boundary elements. It is a bit different from the conventional boundary elements. Typically, a Newton iteration method is used to find the minimum distance point, starting from an arbitrary point on the element with intrinsic coordinates (ξ, η). The iterative increment vector $\{\Delta\xi,\ \Delta\eta\}^{\mathrm{T}}$ is determined by solving the following system:

$$\begin{bmatrix}\frac{\partial x_i}{\partial\xi}\cdot\frac{\partial x_i}{\partial\xi}+r_i\cdot\frac{\partial^2 x_i}{\partial\xi^2} & \frac{\partial x_i}{\partial\xi}\cdot\frac{\partial x_i}{\partial\eta}+r_i\cdot\frac{\partial^2 x_i}{\partial\xi\partial\eta}\\ \frac{\partial x_i}{\partial\xi}\cdot\frac{\partial x_i}{\partial\eta}+r_i\cdot\frac{\partial^2 x_i}{\partial\xi\partial\eta} & \frac{\partial x_i}{\partial\eta}\cdot\frac{\partial x_i}{\partial\eta}+r_i\cdot\frac{\partial^2 x_i}{\partial\eta^2}\end{bmatrix}\begin{Bmatrix}\Delta\xi\\ \Delta\eta\end{Bmatrix}=-\begin{Bmatrix}r_i\cdot\frac{\partial x_i}{\partial\xi}\\ r_i\cdot\frac{\partial x_i}{\partial\eta}\end{Bmatrix}, \tag{24}$$

in which the repeated subscripts i imply summations, ranging from 1 to 3; r_i represents the distance of i th direction from the source point to the trial point. Generally, the iteration times won't exceed 6 when the minimum distance point is found. However, for sphere elements, two stationary points, one a minimum distance and the other a maximum, exist. If the iteration converges to the intrinsic coordinates (ξ_m, η_m), the distance from the source point to the opposite coordinates ($\xi_m \pm 1$, $\eta_m \pm 1$) should also be compared, with the smaller distance selected as the minimum.

The essence of the element subdivision method is to divide the element into several sub-elements, thereby reducing the element length L and satisfying the condition in Eq. (22). This subdivision prevents the integrand from changing too abruptly over the integration range, transforming Eq. (22) to obtain the length of each sub-element:

$$L=4r\left(\frac{e}{2}\right)^{p/(2m)}, \tag{25}$$

where r represents the minimum distance from the source point to the sub-element. This distance changes as subdivision proceeds, meaning that sub-element lengths are adaptive and vary according to the distance, hence the term "adaptive element subdivision method". For both sphere and poleless sphere elements, subdivisions are carried out along the latitude ξ and longitude η directions, as follows:

1) Calculate the actual lengths L_ξ and L_η of the sphere element along ξ and η directions, respectively. Determine the minimum distance $r_{\min}$ and intrinsic coordinate (ξ_A, η_A) of the nearest point A on the element.
2) Based on L_ξ, L_η and $r_{\min}$, verify if the conditions for both directions in Eq. (22) are met. If neither condition holds, subdivision is unnecessary for this source point. If one or both conditions are met, begin the subdivision process.
3) Let $r_{\min}$ be r, calculate L using Eq. (25), and locate the first subdivision point along the ξ^+ direction. (That means the first subdivision point is located at a distance L from point A along ξ^+ direction.)
4) Calculate the distance between the source point P and the latest subdivision point, denoted by r_n. With r_n be r, determine L by Eq. (25) for the n-th sub-element along ξ^+ direction and locate the next subdivision point. (The next subdivision point is located at a distance L from the latest subdivision point along ξ^+ direction.) If the intrinsic coordinate of this point exceeds $\xi_A + 1$, set it to $\xi_A + 1$ and halt the subdivision along ξ^+ direction.
5) Similarly, repeat steps 3 and 4 along ξ^-, η^+ and η^-directions.

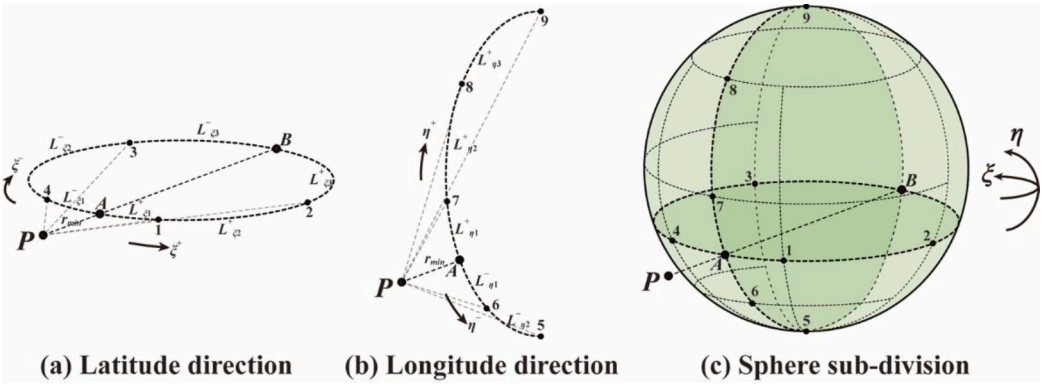

Fig. 12. Adaptive element subdivision for a sphere element.

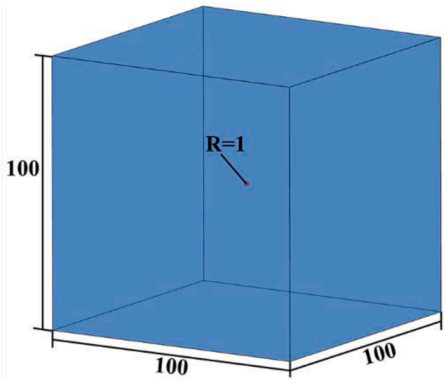

Fig. 13. Computational model of the example 1.

6) Using the subdivision points in these four directions, divide the sphere element into several sub-elements, as shown in Fig. 12(c) (Just one possible subdivision result).

In Fig. 12, subdivision points are numbered 1–9, excluding the closest point *A* and the farthest point *B*. Note that some sub-elements are merged if they are sufficiently far from the source point to satisfy Eq. (22). For poleless sphere elements, the subdivision is similar and thus not shown in detail.

5. Numerical examples

To show the performance of sphere and poleless sphere elements and to verify the correctness of the integration techniques, three numerical examples are given in this section, which place emphasis on the physical variables over the spheres.

5.1. Cube with single spherical void

The first example considers a cube containing a single spherical void, focusing on the stress results across the spherical surface and comparing the accuracy of various discretization methods with the exact solution. The size of the cube is 100×100×100. The radius of the spherical void is 1, positioned at the center of the cube, as shown in Fig. 13. For convenience, the origin of coordinate system is established at center of the void, with three axes aligned parallel to the edges of the cube. The stress distributions throughout the entire cube are as follows:

$$\begin{aligned}\sigma_r(r) &= q\left(1-\frac{R^3}{r^3}\right)\\ \sigma_t(r) &= q\left(1+\frac{R^3}{2r^3}\right)\\ \tau_{rt}(r) &= 0\end{aligned}, \tag{26}$$

in which q implies the tractions at infinity, and is set to 1; R is the radius of the spherical void; r is the distance from a point within the computational domain to the center of the sphere. These formulas are also the exact solution for the stress distribution in the problem of a spherical void within an infinite domain. However, in this model, the domain is truncated at the surface of the cube rather than extending to infinity. Consequently, the stresses obtained from Eq. (26) are used to calculate the surface tractions at the truncation surfaces through the coordinate transformation of the stress tensor and the relationship between surface tractions and stresses. The calculated surface tractions are then applied as boundary conditions on the model's outer surfaces.

In total, 10 kinds of boundary element models are employed in this example. All models share the same mesh on the six outer surfaces of the cube, while the discretization methods of the spherical voids are different. The spherical voids are discretized as follows: 6-node, 14-node, 26-node, 62-node and 114-node sphere elements (corresponding to models 1–5, respectively), a 12-node poleless sphere element combined with 8 linear triangular elements (model 6, 14 nodes in total), a 40-node poleless sphere element with 8 quadratic triangular elements (model 7, 60 nodes in total), a 84-node poleless sphere element with 12 quadratic triangular elements (model 8, 98 nodes in total), 24 conventional 8-node boundary elements (model 9, 74 nodes in total, as shown in Fig. 14(a)), and 96 conventional 8-node boundary elements (model 10, 290 nodes in total, as shown in Fig. 14(b)).

After calculation, the maximum and average values of von Mises stress errors over the spherical voids are listed in Table 1. The errors are calculated as follows:

$$error = \left|\frac{\sigma_c - \sigma_{exact}}{\sigma_{exact}}\right| \times 100\%, \tag{27}$$

in which σ_c and σ_{exact} are the calculated and exact von Mises stress, respectively. According to Eq. (26), $\sigma_{exact} = 1.5$ on the spherical void. Meanwhile, the maximum and average values of von Mises stress errors over spheres with radii of 1.3 are listed in Table 2, derived from the statistics of 182 points on these spheres. As can be seen from Table 1, the maximum error is 3.365% by using 24 conventional 8-node quadratic boundary elements (74 nodes), while it can be reduced to 0.723% by using 40-node poleless sphere elements combined with 8 quadratic triangular elements (50 nodes). In Table 2, for spheres with radii of 1.3,

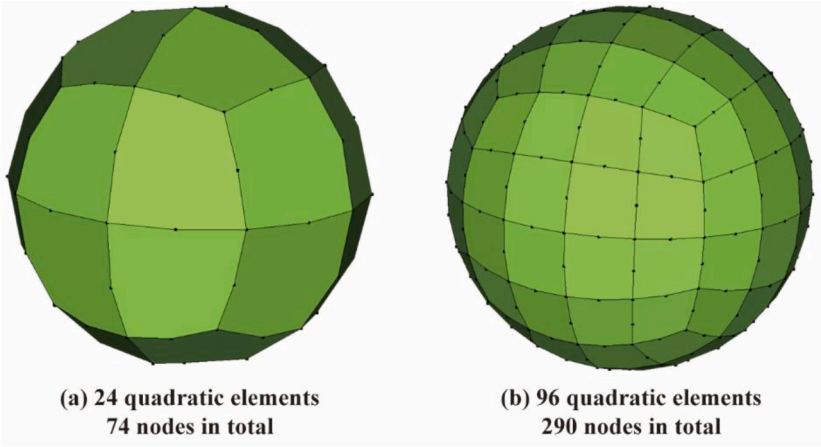

Fig. 14. Two conventional discretization methods of the spherical void.

Table 1
Von-Mises stress errors over spherical voids of 10 models.

Model	Number of nodes on sphere	Maximum errors	Average errors	Model	Number of nodes on sphere	Maximum errors	Average errors
Model 1	6	31.629%	10.543%	Model 6	14	5.547%	3.081%
Model 2	14	31.629%	4.518%	Model 7	50	0.723%	0.305%
Model 3	26	31.629%	2.433%	Model 8	98	0.575%	0.110%
Model 4	62	31.626%	1.022%	Model 9	74	3.365%	2.171%
Model 5	114	31.512%	0.667%	Model 10	290	0.225%	0.190%

Table 2
Von-Mises stress errors at sphere $r = 1.3$ of 10 models.

Model	Number of nodes on sphere	Maximum errors	Average errors	Model	Number of nodes on sphere	Maximum errors	Average errors
Model 1	6	100.000%	1.610%	Model 6	14	19.511%	0.893%
Model 2	14	100.000%	1.610%	Model 7	50	1.405%	0.512%
Model 3	26	100.000%	1.610%	Model 8	98	1.374%	0.511%
Model 4	62	100.000%	1.061%	Model 9	74	8.511%	5.196%
Model 5	114	100.000%	1.055%	Model 10	290	0.538%	0.363%

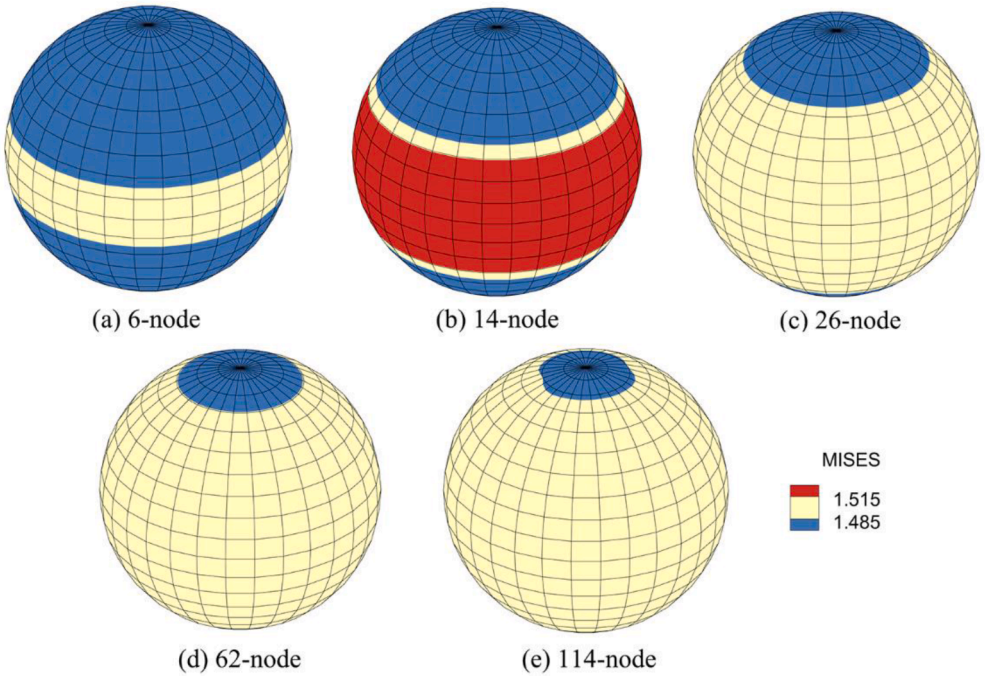

Fig. 15. Von-Mises stress contours over the spherical voids for all sphere elements.

two maximum errors are 8.511% and 1.405%, respectively. These two groups of maximum errors sufficiently manifest the accuracy of the poleless sphere elements. In addition, it can also be found that the maximum errors of all sphere elements are about 31% over the spherical voids and 100% over the spheres with radii of 1.3. The average errors decrease as the number of nodes in elements increases. This is due to the fact that the maximum errors consistently occur at two polar nodes and their vicinity due to zero Jacobians. As the interpolation order increases, the errors of other nodes decrease, leading to a reduction in average errors. In order to illustrate this, von Mises stress contours over the spherical voids are drawn in Fig. 15. In Fig. 15, the yellow region indicates that von Mises stress values range from 1.485 to 1.515, meaning the error is less than 1%. It can be inferred that the sphere elements may perform better if the zero Jacobian problem is resolved.

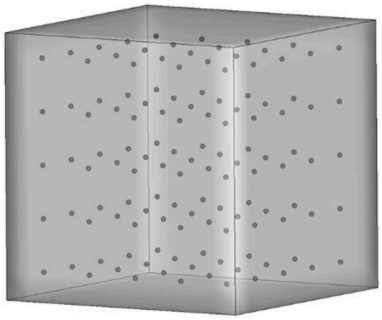

Fig. 16. Computational model of the example 2.

5.2. *Cube with even-distributed spherical voids*

The second example considers a 100×100×100 cube with 125 (5 × 5 × 5) evenly distributed spherical voids, each with a radius of 1. The distance between two adjacent voids is 20, as shown in Fig. 16. The center of the cube serves as the origin of the coordinate system, with the *x, y, z* axes parallel to the cube's edges. The upper surface of the cube is subjected to a uniformly distributed pressure of 1.5, while the bottom surface is fixed. The main purpose of this example is to demonstrate the

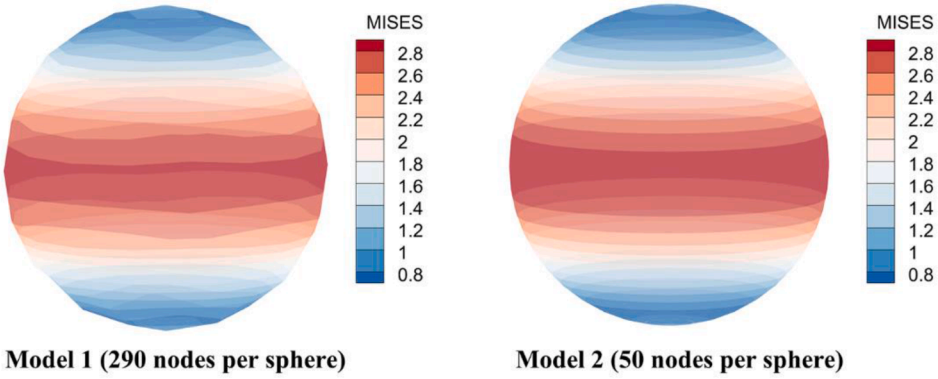

Fig. 17. Von-Mises stresses over one spherical void.

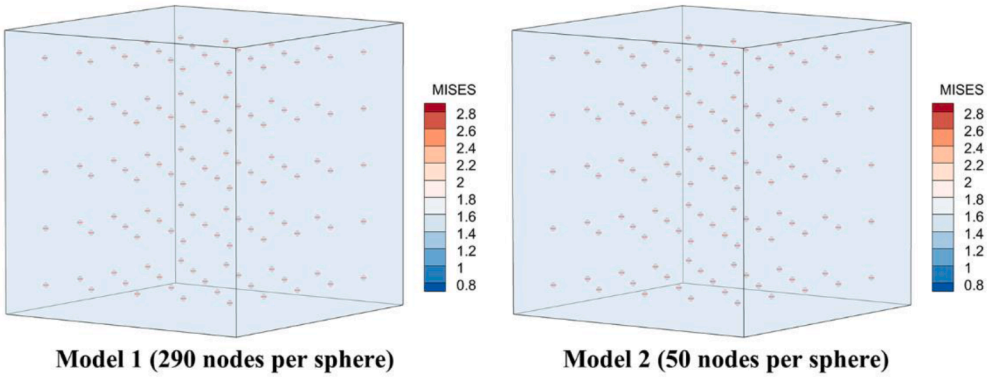

Fig. 18. Von-Mises stress contours of two models.

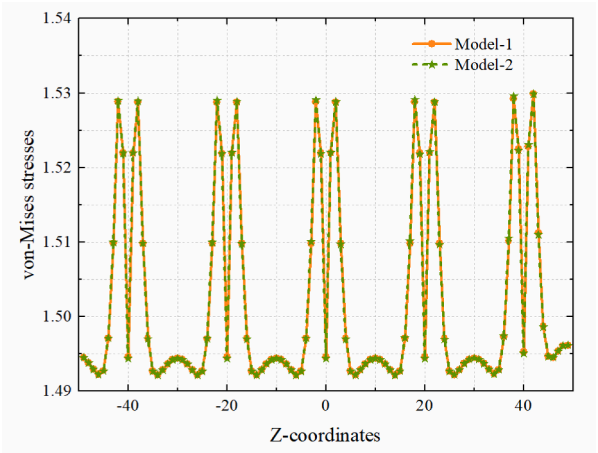

Fig. 19. Von-Mises stresses on the line $x = y = 2$.

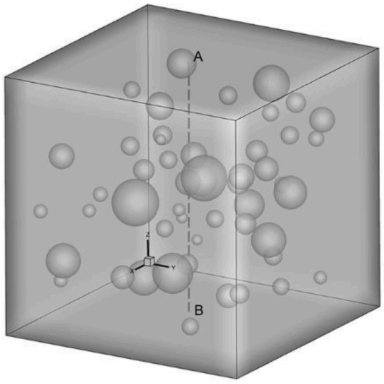

Fig. 20. Computational model of example 3.

effectiveness of the poleless sphere elements in handling computational models with multiple spherical voids. In this example, the voids are discretized in two ways, while the cube surfaces are discretized in the same way. In model 1, 96 quadratic elements are employed to discretize each sphere (290 nodes for one sphere). In model 2, each sphere is discretized using a 40-node poleless sphere element combined with 8 quadratic triangular elements (50 nodes for one sphere). The total node counts for models 1 and 2 are 38,052 and 8052, respectively.

After the calculations, the von Mises stresses over the spherical void located at the center of the models are shown in Fig. 17. The von Mises stress contours for two models are shown in Fig. 18. To compare the results of two models in detail, von Mises stresses along the line $x = y = 2$ are extracted and plotted in Fig. 19. These three figures indicate that the stress results for the two models are nearly identical, confirming that poleless sphere elements can effectively address cases with multiple spherical voids. However, the DOFs of model 1 are approximately 4.7 times greater than those of model 2. The computational times of models 1 and 2 are about 901 min and 24 min, respectively, demonstrating the efficiency of the poleless sphere elements.

5.3. *Cube with randomly distributed spherical inclusions*

The main purpose of the third example is to demonstrate the capability of poleless sphere elements in simulating arbitrarily distributed spheres and dealing with multi-media models. In this example, a cube with randomly distributed spherical inclusions is considered. The sizes

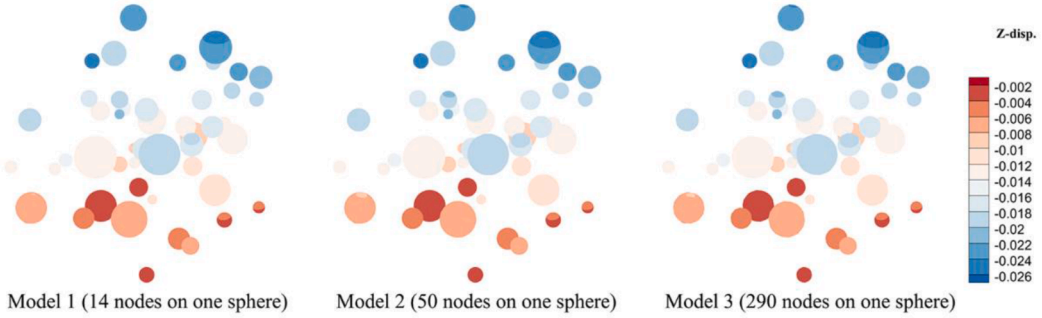

Fig. 21. Z-displacement distribution over the sphere inclusions.

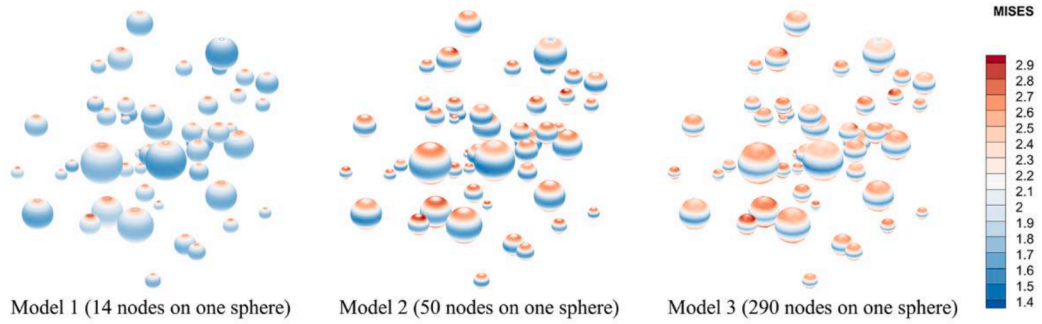

Fig. 22. Von-Mises stress distribution over the sphere inclusions.

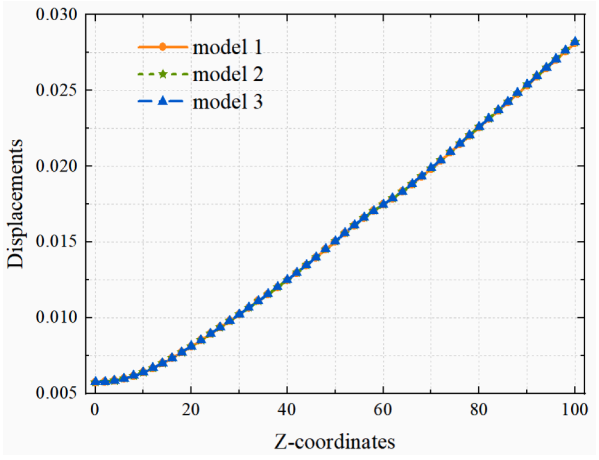

Fig. 23. Displacements along line AB.

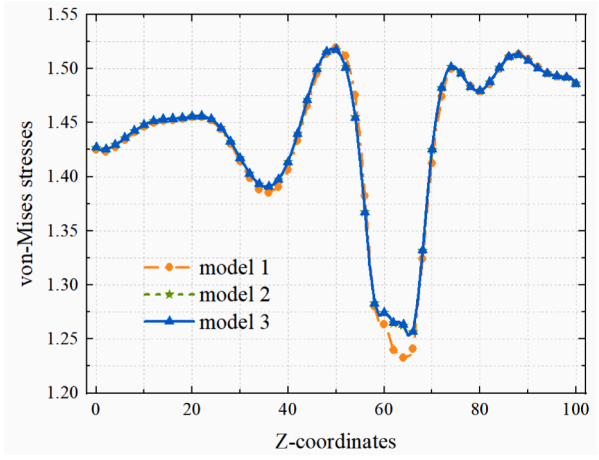

Fig. 24. Von-Mises stresses along line AB.

and positions of the spherical inclusions are generated by computer random numbers. The entire model is shown in Fig. 20. Line AB in the figure does not intersect any inclusions and will be referenced for result comparison. The boundary conditions of the cube remain consistent with those in example 2. The shear modulus and Poisson ratio of the inclusions are 30,000 and 0.25, respectively, while those of substrate material are 2000 and 0.3, respectively. Due to the involvement of two materials, the multi-domain boundary element method (MDBEM) [27–29] is employed for calculations.

Three discretization models are used in this example. Each inclusion of model 1 is discretized by a 12-node poleless sphere element combined with 8 linear triangular elements (14 nodes per inclusion). In Model 2, inclusions are discretized by 40-node poleless sphere elements with 8 quadratic triangular elements (50 nodes per inclusion). In Model 3, each inclusion is discretized by 96 8-node elements (290 nodes per inclusion). The discretization of six outer surfaces of the cube remains the same across all three models. The total number of nodes for models 1, 2, and 3 are 2502, 4302 and 16,302, respectively. According to the tests that are not shown here, model 3 is sufficiently refined to provide reliable results for this problem, and its outcomes are considered the standard reference.

After the calculations, the displacement and von Mises stress results of three models are obtained. The displacement and von Mises stress contours are shown in Fig. 21 and Fig. 22, respectively. Meanwhile, the displacements and von Mises stresses along line AB have been extracted and plotted in Fig. 23 and Fig. 24, respectively. It is evident that the displacement results of three models are nearly identical, while the stress results of model 2 and model 3 show close agreement. However, the stress results of model 1 has significant difference from those of model 3. This indicates that the combination of the 12-node poleless sphere element and 8 linear triangular elements may be sufficient for accurate displacement calculations, but not for stress evaluations. If the

focus is solely on displacement results in such structures, a single spherical inclusion requires only 14 nodes. Conversely, if the stress distribution is of interest, a spherical inclusion may necessitate 50 nodes. The computational times of models 1, 2 and 3 are about 2.5 min, 11 min and 765 min, respectively.

6. Conclusions

In this paper, sphere elements and poleless sphere elements are proposed. Sphere elements are constructed by the semi-hole elements and hole elements, while poleless sphere elements are constructed by the arc elements and hole elements. Usually, poleless sphere elements are combined with several triangular elements to simulate the spherical surface. To accurately evaluate all types of singular integrals over these newly proposed elements, various techniques are employed. The rigid body motion method is applied to evaluate strong-singular integrals. Weak-singular integrals are addressed using the degenerate element method, while near-singular integrals are calculated through adaptive element subdivision methods. Finally, three examples demonstrate the effective performance of poleless sphere elements. The discussions and conclusions are summarized as follows:

1. When addressing weak-singular integrals using the degenerate element method, it is essential first to map the sphere or poleless sphere elements onto a square. This mapping process differs from that used in conventional boundary elements.
2. For two kinds of sphere elements, element subdivision along latitude direction should always proceed from the minimum distance point to the opposite point, ensuring that each subsequent subdivision point is farther from the source point than the last.
3. Due to the zero Jacobians at the two poles, sphere elements can produce significant errors when simulating spherical geometries at these locations. Except for the two poles, the stress errors at other nodes decrease as the interpolation order increases, which underscores the need for poleless sphere elements.
4. Combined with several triangular elements, poleless sphere elements have good accuracy in simulating spherical geometries. In structures with numerous spherical voids or inclusions, they can achieve accurate stress results using 50 nodes per sphere and accurate displacement results with just 14 nodes per sphere, significantly reducing the number of degrees of freedom (DOFs) compared to conventional 8-node boundary elements.

CRediT authorship contribution statement

Yong-Tong Zheng: Writing – review & editing, Writing – original draft, Validation, Software, Methodology, Funding acquisition, Data curation, Conceptualization. **Yijun Liu:** Writing – review & editing, Supervision, Software, Methodology, Funding acquisition. **Xiao-Wei Gao:** Writing – review & editing, Software, Methodology, Investigation, Funding acquisition, Conceptualization. **Wei-Zhe Feng:** Writing – review & editing, Software, Funding acquisition.

Declaration of competing interest

The authors declare that they have no competing of interests.

Acknowledgment

The supports of this investigation by the National Natural Science Foundation of China (Grant Nos. 12302261, 12372198, 12072064) and National Key Laboratory of Electromagnetic Energy (614221723010104) are gratefully acknowledged.

Appendix A. The shape functions and diagrams of trigonometric semi-hole elements

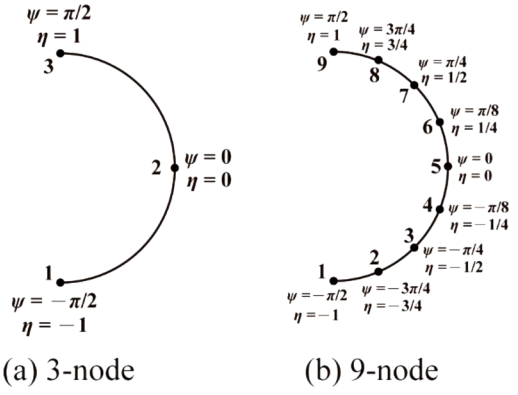

Fig. 25. The diagrams of 3-node and 9-node trigonometric semi-hole elements.

The shape functions of 3-node trigonometric semi-hole element (as shown in Fig. 25(a)):

$$N_1(\psi) = \frac{1}{2} - \frac{1}{2}\cos\psi - \frac{1}{2}\sin\psi$$

$$N_2(\psi) = \cos\psi$$

$$N_3(\psi) = \frac{1}{2} - \frac{1}{2}\cos\psi + \frac{1}{2}\sin\psi$$

The shape functions of 9-node trigonometric semi-hole element (as shown in Fig. 25(b)):

$$N_1(\psi)= 2\cos^4\psi - \left(2+\sqrt{2}+\sqrt{4+2\sqrt{2}}\right)\cos^3\psi + \left(\frac{3\sqrt{2}}{2}+\sqrt{10+7\sqrt{2}}\right)\cos^2\psi - \left(\frac{1+\sqrt{2}}{2}+\sqrt{2+\sqrt{2}}\right)\cos\psi + 2\cos^3\psi\sin\psi - \left(\sqrt{2}+\sqrt{4+2\sqrt{2}}\right)\cos^2\psi\sin\psi + \left(\frac{\sqrt{2}}{2}+\sqrt{2+\sqrt{2}}\right)\cos\psi\sin\psi - \frac{1}{2}\sin\psi + \frac{1}{2}$$

$$N_2(\psi) = -\left(4+2\sqrt{2}+\sqrt{16+8\sqrt{2}}\right)\cos^4\psi + \left(8+6\sqrt{2}+\sqrt{116+82\sqrt{2}}\right)\cos^3\psi - \left(6+5\sqrt{2}+\sqrt{106+73\sqrt{2}}\right)\cos^2\psi + \left(2+\sqrt{2}+\sqrt{10+7\sqrt{2}}\right)\cos\psi - \left(2\sqrt{2}+\sqrt{16+8\sqrt{2}}\right)\cos^3\psi\sin\psi + \left(4+2\sqrt{2}+\sqrt{20+14\sqrt{2}}\right)\cos^2\psi\sin\psi - \left(2+\sqrt{2}+\sqrt{2+\sqrt{2}}\right)\cos\psi\sin\psi$$

$$N_3(\psi) = \left(8+6\sqrt{2}+4\sqrt{10+7\sqrt{2}}\right)\cos^4\psi - \left(20+14\sqrt{2}+2\sqrt{194+137\sqrt{2}}\right)\cos^3\psi + \left(15+10\sqrt{2}+\sqrt{2\left(194+137\sqrt{2}\right)}\right)\cos^2\psi - \left(3+2\sqrt{2}+\sqrt{20+14\sqrt{2}}\right)\cos\psi - \left(4+4\sqrt{2}+2\sqrt{10+7\sqrt{2}}\right)\cos^2\psi\sin\psi + \left(4+2\sqrt{2}+4\sqrt{2+\sqrt{2}}\right)\cos^3\psi\sin\psi + \left(1+\sqrt{2}+\sqrt{4+2\sqrt{2}}\right)\cos\psi\sin\psi$$

$$N_4(\psi) = -\left(16+10\sqrt{2}+2\sqrt{116+82\sqrt{2}}\right)\cos^4\psi + \left(32+22\sqrt{2}+\sqrt{2020+1426\sqrt{2}}\right)\cos^3\psi - \left(20+15\sqrt{2}+\sqrt{850+601\sqrt{2}}\right)\cos^2\psi + \left(4+3\sqrt{2}+\sqrt{34+23\sqrt{2}}\right)\cos\psi - \left(4+2\sqrt{2}+2\sqrt{4+2\sqrt{2}}\right)\cos^3\psi\sin\psi + \left(4+2\sqrt{2}+\sqrt{20+14\sqrt{2}}\right)\cos^2\psi\sin\psi - \left(\sqrt{2}+\sqrt{2+\sqrt{2}}\right)\cos\psi\sin\psi$$

$$N_5(\psi) = \left(20+12\sqrt{2}+8\sqrt{10+7\sqrt{2}}\right)\cos^4\psi - \left(36+26\sqrt{2}+2\sqrt{676+478\sqrt{2}}\right)\cos^3\psi + \left(22+17\sqrt{2}+2\sqrt{274+193\sqrt{2}}\right)\cos^2\psi - \left(5+3\sqrt{2}+2\sqrt{10+7\sqrt{2}}\right)\cos\psi$$

$$N_6(\psi) = -\left(4+2\sqrt{2}+\sqrt{16+8\sqrt{2}}\right)\cos^4\psi + \left(8+6\sqrt{2}+\sqrt{116+82\sqrt{2}}\right)\cos^3\psi - \left(6+5\sqrt{2}+\sqrt{106+73\sqrt{2}}\right)\cos^2\psi + \left(2+\sqrt{2}+\sqrt{10+7\sqrt{2}}\right)\cos\psi + \left(2\sqrt{2}+\sqrt{16+8\sqrt{2}}\right)\cos^3\psi\sin\psi - \left(4+2\sqrt{2}+\sqrt{20+14\sqrt{2}}\right)\cos^2\psi\sin\psi + \left(2+\sqrt{2}+\sqrt{2+\sqrt{2}}\right)\cos\psi\sin\psi$$

$$N_7(\psi) = \left(8+6\sqrt{2}+4\sqrt{10+7\sqrt{2}}\right)\cos^4\psi - \left(20+14\sqrt{2}+2\sqrt{194+137\sqrt{2}}\right)\cos^3\psi + \left(15+10\sqrt{2}+\sqrt{2\left(194+137\sqrt{2}\right)}\right)\cos^2\psi - \left(3+2\sqrt{2}+\sqrt{20+14\sqrt{2}}\right)\cos\psi + \left(4+4\sqrt{2}+2\sqrt{10+7\sqrt{2}}\right)\cos^2\psi\sin\psi - \left(4+2\sqrt{2}+4\sqrt{2+\sqrt{2}}\right)\cos^3\psi\sin\psi - \left(1+\sqrt{2}+\sqrt{4+2\sqrt{2}}\right)\cos\psi\sin\psi$$

$$N_8(\psi) = -\left(4+2\sqrt{2}+\sqrt{16+8\sqrt{2}}\right)\cos^4\psi + \left(8+6\sqrt{2}+\sqrt{116+82\sqrt{2}}\right)\cos^3\psi - \left(6+5\sqrt{2}+\sqrt{106+73\sqrt{2}}\right)\cos^2\psi + \left(2+\sqrt{2}+\sqrt{10+7\sqrt{2}}\right)\cos\psi + \left(2\sqrt{2}+\sqrt{16+8\sqrt{2}}\right)\cos^3\psi\sin\psi - \left(4+2\sqrt{2}+\sqrt{20+14\sqrt{2}}\right)\cos^2\psi\sin\psi + \left(2+\sqrt{2}+\sqrt{2+\sqrt{2}}\right)\cos\psi\sin\psi$$

$$N_9(\psi) = 2\cos^4\psi - \left(2+\sqrt{2}+\sqrt{4+2\sqrt{2}}\right)\cos^3\psi + \left(\frac{3\sqrt{2}}{2}+\sqrt{10+7\sqrt{2}}\right)\cos^2\psi - \left(\frac{1+\sqrt{2}}{2}+\sqrt{2+\sqrt{2}}\right)\cos\psi - 2\cos^3\psi\sin\psi + \left(\sqrt{2}+\sqrt{4+2\sqrt{2}}\right)\cos^2\psi\sin\psi - \left(\frac{\sqrt{2}}{2}+\sqrt{2+\sqrt{2}}\right)\cos\psi\sin\psi + \frac{1}{2}\sin\psi + \frac{1}{2}$$

Data availability

The raw/processed data required to reproduce these findings cannot be shared at this time as the data also forms part of an ongoing study.

References

[1] Zienkiewicz OC, Taylor RL. The finite element method. 6th ed. London: Elsevier; 2005.
[2] Liu GR, Quek SS. The finite element method: a practical course. second. Oxford, UK: Butterworth-Heinemann Elsevier; 2003.
[3] Hughes TJR. The finite element method: linear static and dynamic finite element analysis. Englewood Cliffs, N.J.: Prentice-Hall; 1987.
[4] Liu Y. Fast multipole boundary element method: theory and applications in engineering. Cambridge: Cambridge University Press; 2009.
[5] Brebbia CA, Dominguez J. Boundary elements: an introductory course. Southampton: Computational Mechanics Publications; 1992.
[6] Gao XW, David TG. Boundary element programming in mechanics. Cambridge, UK: Cambridge University Press; 2002.
[7] Feng J, Yao Z, Liu Y, Zou Y, Zheng X. Some spherical boundary elements and a discretization error indicator for acoustic problems with spherical surfaces. Eng Anal Bound Elem 2015;56:176–89. https://doi.org/10.1016/j.enganabound.2015.01.018.
[8] Gao XW, Zeng WH, Cui M. Isoparametric tube elements and their application in heat conduction BEM analysis. Chin J Comput Mech 2016;33:328–34. https://doi.org/10.7511/jslx201603008.
[9] Gao XW, Yuan ZC, Peng HF, Cui M, Yang K. Isoparametric closure elements in boundary element method. Comput Struct 2016;168:1–15. https://doi.org/10.1016/j.compstruc.2016.02.002.
[10] Gao XW, Zheng YT, Peng HF, Cui M, Zhang ZY. Trans-accuracy elements and their application in BEM analysis of structurally multi-scale problems. Eng Anal Bound Elem 2018;97:82–93. https://doi.org/10.1016/j.enganabound.2018.09.011.
[11] Ma H, He D, Tian Y. High order isoparametric elements in boundary element method—Smooth spheroidal element. Eng Anal Bound Elem 2019;104:34–45. https://doi.org/10.1016/j.enganabound.2019.03.019.
[12] Ma H, Tian Y, He D. High order isoparametric elements in boundary element method–smooth elliptical element. Eng Anal Bound Elem 2019;101:37–47. https://doi.org/10.1016/j.enganabound.2018.12.009.
[13] Henry DP, Ma F, Chatterjee J, Banerjee PK. Steady state thermoelastic analysis of 3D solids with fiber inclusions by boundary element method. Comput Methods Appl Mech Eng 2007;197:294–307. https://doi.org/10.1016/j.cma.2007.08.001.
[14] Banerjee PK, Henry DP. Elastic analysis of three-dimensional solids with fiber inclusions by BEM. Int J Solids Struct 1992;29:2423–40. https://doi.org/10.1016/0020-7683(92)90001-A.
[15] Henry DP, Banerjee PK. Elastic stress analysis of three-dimensional solids with small holes by BEM. Int J Numer Methods Eng 1991;31:369–84. https://doi.org/10.1002/nme.1620310210.
[16] Chatterjee J, Henry DP, Ma F, Banerjee PK. An efficient BEM formulation for three-dimensional steady-state heat conduction analysis of composites. Int J Heat Mass Transf 2008;51:1439–52. https://doi.org/10.1016/j.ijheatmasstransfer.2007.09.004.
[17] Buroni FC, Marczak RJ. Effective properties of materials with random micro-cavities using special boundary elements. J Mater Sci 2008;43:3510–21. https://doi.org/10.1007/s10853-008-2479-3.
[18] Buroni FC, Marczak RJ. A family of hole boundary elements for modeling materials with cylindrical voids. Eng Anal Bound Elem 2008;32:578–90. https://doi.org/10.1016/j.enganabound.2007.11.003.
[19] Huang C, Zhang J, Qin X, Lu C, Sheng X, Li G. Stress analysis of solids with open-ended tubular holes by BFM. Eng Anal Bound Elem 2012;36:1908–16. https://doi.org/10.1016/j.enganabound.2012.07.009.
[20] Qin X, Zhang J, Liu L, Li G. Steady-state heat conduction analysis of solids with small open-ended tubular holes by BFM. Int J Heat Mass Transf 2012;55:6846–53. https://doi.org/10.1016/j.ijheatmasstransfer.2012.06.091.
[21] Wang X, Lu C, Zhou F, Zheng X, Zhang J. Acoustic problems analysis of 3D solid with small holes by fast multipole boundary face method. Eng Anal Bound Elem 2013;37:1703–11. https://doi.org/10.1016/j.enganabound.2013.09.013.
[22] Zheng YT, Liu Y, Gao XW, Yang Y, Peng HF. Improved hole and tube elements in BEM for elasticity problems. Eng Anal Bound Elem 2024;159:17–35. https://doi.org/10.1016/j.enganabound.2023.11.021.
[23] Dumont NA. The boundary element method revisited. In: C.A. B, editors. Boundary elements and other mesh reduction methods XXXII, 50. Southampton: WIT Press; 2010. p. 227–38. https://doi.org/10.2495/BE100201.
[24] Dumont NA. The collocation boundary element method revisited: perfect code for 2d problems. Int J Comput Methods Exp Meas 2018;6:965–75. https://doi.org/10.2495/CMEM-V6-N6-965-975.
[25] Dumont NA. The consistent boundary element method for potential and elasticity: part I–formulation and convergence theorem. Eng Anal Bound Elem 2023;149:127–42. https://doi.org/10.1016/j.enganabound.2023.01.017.
[26] Gao XW, Yang K, Wang J. An adaptive element subdivision technique for evaluation of various 2D singular boundary integrals. Eng Anal Bound Elem 2008;32:692–6. https://doi.org/10.1016/j.enganabound.2007.12.004.
[27] Gao XW, Guo L, Zhang C. Three-step multi-domain BEM solver for nonhomogeneous material problems. Eng Anal Bound Elem 2007;31:965–73. https://doi.org/10.1016/j.enganabound.2007.06.002.
[28] Peng HF, Bai YG, Yang K, Gao XW. Three-step multi-domain BEM for solving transient multi-media heat conduction problems. Eng Anal Bound Elem 2013;37:1545–55. https://doi.org/10.1016/j.enganabound.2013.08.012.
[29] Zheng YT, Gao XW, Peng HF, Xu BB. The coupled method of multi-domain BEM and element differential method for solving multi-scale problems. Eng Anal Bound Elem 2020;113:145–55. https://doi.org/10.1016/j.enganabound.2020.01.001.